



Design of a Morphing Airfoil with Composite Chiral Structure

Alessandro Airoldi,* Marco Crespi,† Giuseppe Quaranta,‡ and Giuseppe Sala§
Politecnico di Milano, 20156 Milan, Italy

DOI: 10.2514/1.C031486

The paper presents a design study for a morphing structural concept, which could be used to obtain a passively actuated high-lift wing configuration. A composite chiral honeycomb core is used to allow large variations of camber at limited strain levels in the structure of the aerodynamic surface. The design hypothesis is first assessed by means of structural analyses, which are performed applying two-dimensional and three-dimensional finite elements schemes. The results confirm the morphing capabilities in the chordwise direction of the structure, which still retains noteworthy axial and torsional stiffness properties. The aeroelastic performances of the morphing airfoil are then optimized, taking into account aeroelastic stability as well as strength constraints. The optimal parameters of chiral network and the required stiffness properties of the covering skin are identified. Overall, the work confirms the promising performances of morphing structures based on chiral topologies and assesses a numerical approach for the design of morphing aerodynamic structures.

Nomenclature

A, B, D	= stiffness coefficient matrices of laminate
C_L	= lift coefficient
$C_{L\alpha}$	= lift-curve slope
C_p	= pressure coefficient
c	= chord
D_{skin}	= flexural stiffness of the morphing skin
E	= Young's modulus
\mathbf{F}^a	= generalized aerodynamic force vector
G	= shear modulus
\mathbf{H}_{am}	= transfer function matrix of unsteady generalized aerodynamic forces
L	= length of chiral ligaments
\mathbf{K}_s	= structural modal stiffness matrix
\mathbf{M}	= out-of-plane bending moment vector for laminate
M_b	= bending moment in chiral ligaments
\mathbf{M}_s	= structural modal mass matrix
\mathbf{N}	= in-plane force vector for laminate
\mathbf{q}	= vector of generalized modal structural coordinates
q	= dynamic pressure
R	= distance between chiral node centers of the same cell
r	= radius of chiral node
t_c	= thickness of composite laminate for chiral ligaments
\mathbf{u}	= nodal displacement vector
\mathbf{x}_a	= state vector of unsteady aerodynamic state-space model
x_{g1}	= position of front hinge
x_{g2}	= position of back hinge
x_1	= position of front spar
x_2	= position of back spar
α	= angle of attack

Received 28 April 2011; revision received 14 September 2011; accepted for publication 14 November 2011. Copyright © 2011 by Politecnico di Milano. Published by the American Institute of Aeronautics and Astronautics, Inc., with permission. Copies of this paper may be made for personal or internal use, on condition that the copier pay the \$10.00 per-copy fee to the Copyright Clearance Center, Inc., 222 Rosewood Drive, Danvers, MA 01923; include the code 0021-8669/12 and \$10.00 in correspondence with the CCC.

*Assistant Professor, Dipartimento di Ingegneria Aerospaziale, Via La Masa, 34; alessandro.airoldi@polimi.it.

†Graduate Student, Dipartimento di Ingegneria Aerospaziale, Via La Masa, 34; crespi@aero.polimi.it.

‡Assistant Professor, Dipartimento di Ingegneria Aerospaziale, Via La Masa, 34; giuseppe.quaranta@polimi.it (Corresponding Author).

§Professor, Dipartimento di Ingegneria Aerospaziale, Via La Masa, 34; giuseppe.sala@polimi.it.

β	= tangential angle of ligaments
ϵ	= in-plane strain vector for laminate
ε	= error
κ	= in-plane curvature vector for laminate
ν	= Poisson coefficient
σ_{Cp}^2	= statistical variance of pressure coefficient distribution

I. Introduction

AN AIRCRAFT structure is defined as morphing when it can change its shape and size during flight. Usually, the term morphing refers to seamless shape changes that are continuous and not to classical discrete aircraft wing adaptation systems, such as flaps or leading and trailing-edge high-lift devices. Such types of morphing can be regarded as directly inspired by the imitation of nature, which has been one of the main guidelines for designers since the beginning of human flight [1,2].

The Wright brothers used wing warping on their Flyers to attain control around the roll axis [1]. During the first years of development of aeronautical engineering, the control of wing camber through morphing was considered a feasible mean of lift control [3]. However, the rapid increase of aircraft flight speed and, consequently, of structural air-loads led quickly to the emergence of more reliable and robust systems, such as the movable surfaces that are currently found on aircraft.

Nowadays, the research on direct control of aerodynamic forces through geometrical changes of lifting bodies is again gaining momentum. In principle, a continuous geometric adaptation could provide an extremely efficient and mission-effective aircraft with a reduced fuel consumption that can make it more environmentally friendly. Several concepts have been proposed to move in this direction, such as small-scale deflections of airfoils to increase performance [4–6], variation of wing camber like in the belt-rib concept [7] or in the finger approach proposed in Monner [8], and many others. However, the practical experience with morphing, despite the undoubtedly aerodynamic advantages, has always shown an increase in complexity and weight, most of the time due to the actuation system [9]. Moreover, this effect is usually coupled with a general reduction in the capability of the structure to carry the applied loads. So, great care must be taken in the design of this type of structure because it is easy to obtain structures with a higher susceptibility to detrimental aeroelastic effects like divergence, flutter, or buffet. In fact, the most challenging goal every designer is looking for in morphing aircraft is a structure that can produce large changes in shape while retaining the load-carrying capability. In this paper, an innovative chiral structural assembly is proposed to solve the dilemma, generating a compliant structure chordwise that is able

to withstand the spanwise bending and torsional loads on the wing. Such new topology has been already proposed for decambering airfoils [10,11].

The morphing strategy proposed in this work moves from the capability to build composite chiral networks with improved and adjustable stiffness and strength performances [12]. Such possibility is exploited to investigate the morphing sail concept, i.e., a wing that increase its camber when the angle of attack rises. Morphing, in this case, is realized relying only on wing compliance, without resorting to active actuation systems. The investigation of this passive morphing system allows for focusing on the selection of the optimal trade off between local compliance and global load-carrying capability. However, the sail concept may have practical relevance if applied, for instance, to aircraft vertical fins. In this case, the increase of the lift-curve slope that will result from the airfoil cambering may lead to a reduction of the fin area while keeping the fin volumetric ratio constant [13]. More generally, this behavior may be considered appropriate for high-lift devices.

The paper is organized in seven sections, including this introduction. Section II presents the morphing sail concept. Section III presents the properties of structures based on chiral topology. In Section IV, the load-carrying properties of a chiral wing box are thoroughly analyzed and discussed. Section V shows how numerical aeroelastic models of the morphing sail have been assembled, whereas Section VI presents the optimization procedure used to identify a preliminary design of the structure that takes into account not only the performance but also several aeroelastic constraints. Finally, Section VII summarizes the work done so far and provides recommendations for future developments.

II. Morphing Sail Concept

The possibility of changing the airfoil sectional lift-curve slope is the main driver for the development of any high-lift device currently applied to almost any aircraft. Considering a simple straight airfoil, it is possible to increase the sectional lift curve by an increment of the airfoil camber. If the structure is compliant chordwise, the aerodynamic loads generated by each section depend on the shape taken by the airfoil, which in turn is the result of the deformation of the structure caused by the applied loads. The sectional lift-curve slope becomes, in general, nonlinear because it depends on the dynamic pressure q and the airfoil angle of attack α

$$C_{L\alpha} = C_{L\alpha}(q, \alpha) \quad (1)$$

An advantageous effect is produced when the airfoil behaves like a sail, i.e., for a given angle of attack other than zero, it morphs into a camber geometry, as shown by Fig. 1. It can be expected that the overpressure on the bottom of the airfoil and the depression on the top will promote the shape variation shown in Fig. 1.

When the structure reaches the equilibrium, the newly cambered airfoil has a higher lifting capacity at the same angle of attack as the one shown by the symmetric airfoil, assuming perfect rigidity. The global result is an increment of the lift-curve slope. The behavior of

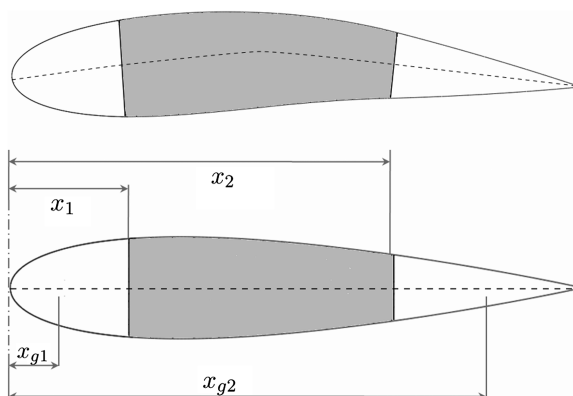


Fig. 1 Morphing sail airfoil concept.

this system resembles that of marine sails. However, the role of these two aerodynamic surfaces is different, and the specific loads carried by the wings are substantially higher than that of marine sails. Wing sections are necessarily thicker than sails, and the wing airfoil has to be substantially rigid thicknesswise.

To achieve the design described here, it is mandatory to 1) join the root section of the wing to the supporting structure through two constraint points separated chordwise to allow the movement described in Fig. 1 from a kinematical point of view; those constraint points can be considered as plain hinges; 2) to adopt a flexible skin, which should provide adequate compliance to allow for large stretching/compression, without failures or permanent plastic deformations; the membranal and flexural stiffness requirements for such skin should be precisely identified before defining suitable engineering solutions; and 3) to design an internal structural frame, which should deform under the action of aerodynamic pressure. Moreover, such an internal structural frame must provide sufficient flexural and torsional stiffness to the wing structure. In fact, the compliant skin will abdicate to the classical role of torsional stiffness supplier for the wing box, so a newly designed element has to provide it.

In the next section, a design hypothesis is presented, which is based on the morphing capability of a chiral network.

III. Chiral Topologies and Skin Solutions for Morphing

A. Properties of Chiral Topologies

Chiral topologies represent an appealing solution for the deformable internal frame of morphing structures. Chiral geometry is based on a noncentrosymmetric topology and consists of an assembly of ligaments and nodes. Figure 2 shows an example of a hexachiral topology with the main geometrical parameters highlighted. From a structural point of view, such topology can be adopted to obtain elements with a tendency to transversally expand when tensed and to transversally contract when compressed [12,14,15].

Hence, an honeycomb or a truss structure with a chiral topology will behave, at the macroscale level, as an auxetic material, with a negative Poisson coefficient that can be close to the theoretical limit of -1 [12,14,15].

An important consequence of such behavior on the mechanical properties is an expected increment of the shear modulus, in accordance with the relation $G = E/2(1 + v)$. The high shear modulus causes the opposition of the structure to the distortion of unit cells; such behavior can be effectively exploited for morphing purposes. In fact, if a displacement is applied to a structure hosting a chiral core, the local inherent resistance to shape changes will lead to a diffused strain state over the entire core, without strain localizations in the weak points of the structure. An important additional feature of

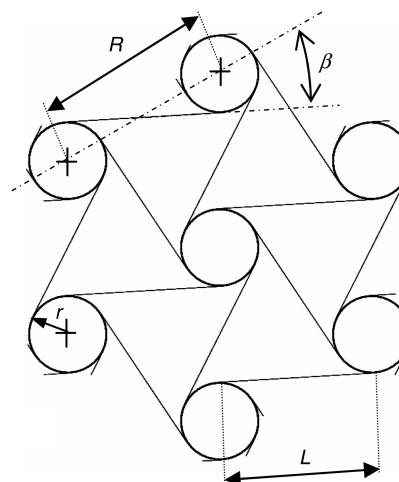


Fig. 2 Chiral cell topology.

chiral topologies is design flexibility, which can be obtained by changing the geometrical parameters (Fig. 2) as well as the ligament thickness and material. Such flexibility allows a fine regulation of structural compliance to meet different morphing behaviors and global stiffness requirements.

Such considerations are at the basis of the adoption of chiral structures for morphing airfoils, which is documented in several works [10–12, 16]. The experimental activities performed on chiral structures manufactured to show morphing capabilities confirmed that these structures can undergo large displacements while keeping the maximum strains at acceptable levels [12].

B. Technology for Composite Chiral Structures

Different manufacturing approaches have been adopted for the production of chiral structures. Airfoils hosting metallic honeycomb cores have been produced by machining light alloy plates [11]. Chiral honeycombs with different geometries have been manufactured by means of rapid prototyping, in acrylonitrile butadiene styrene plastic or polypropylene resin (8040 2 MCP equipment) resin using vacuum casting techniques [17–19]. A chiral wing box was produced in polyamide polymer material and tested in a wind tunnel [16].

The present work was conceived after a novel technological process for the production of carbon composite chiral units, as sketched in Fig. 2, had been created. The process, reported in Bettini et al. [12], starts with the production of laminated ligaments, which are separately cured, and then proceeds by bonding them through an elastomeric tooling technique. The structural response of the hexachiral units was assessed in Bettini et al. [12], proving the capability to undergo large structural displacements without permanent degradation. Moreover, the tensile and compressive tests identified two main failure modes, as shown in Fig. 3. If ligaments are unwound around a node, failure occurs by debonding of the ligament and is not directly related to the stress-strain state inside the ligament. In this case, the value of the unwinding bending moment per unit width at the root of ligament M_b/L could be used to evaluate the risk of such a type of failure. The compressive failure mode is different and can be attributed to the bending failure of the ligaments, which tend to wind around the node. A suitable index for this failure mode is given by longitudinal strain on the ligament surface. The quantitative evaluation of both failure limits was carried out by considering experimental results, strain-gauge acquisitions, and the numerical-experimental correlation with a fully nonlinear and very detailed finite-element (FE) model of the chiral unit [12].

C. Role of the Skin and Modeling Issues for the Identification of its Structural Requirements

The previous works on the application of chiral topologies to morphing aerodynamic surfaces indicate that the structural characteristics of the skin may have an important role on airfoils

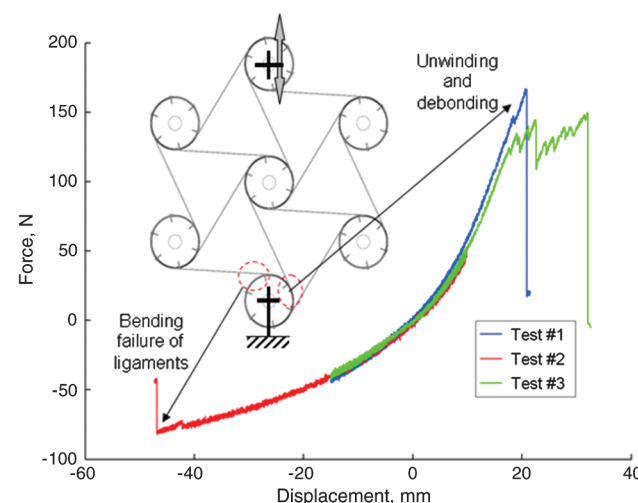


Fig. 3 Response and failure modes of a chiral composite unit.

performance. In the numerical studies carried out by Spadoni and Ruzzene [11], the skin Young's modulus significantly influenced the structural compliance. The polyamide wing box described in Martin et al. [16] was endowed with a 0.5 mm fiberglass skin to reduce the skin's contribution to airfoil stiffness while maintaining adequate stiffness to prevent buckling.

In general, the design of a flexible cover can be regarded as a fundamental issue for the development of effective morphing structural concepts. Several papers present interesting engineering solutions for the skins of morphing structures [20–23]. A review of the literature is presented in Thill et al. [24]. Some basic requirements have been identified in numerical studies, such as in Gandhi and Anusonti-Inthra [20], and can be summarized in three points: 1) the possibility to undergo large recoverable strains, 2) a low membranal stiffness, which reduces the actuation energy, and 3) an adequate flexural stiffness to carry the aerodynamics loads.

Although the present paper is focused on the application of a chiral inner frame to the morphing sail concept, an identification of the maximum strain levels and of stiffness requirements for the skin is important to evaluate the feasibility of the concept as well as to design an adequate solution for the skin.

Based on these considerations, the skin is introduced in the numerical analyses presented in the following sections, but the adopted modeling technique is intended to capture only the overall response, rather than verify the adequacy of a specific engineering solution. For such a reason, the skin is modeled by means of laminated shell elements, which are directly characterized by introducing the stiffness matrix that derives from the application of classical lamination theory:

$$\begin{Bmatrix} \mathbf{N} \\ \mathbf{M} \end{Bmatrix} = \begin{bmatrix} \mathbf{A} & \mathbf{B} \\ \mathbf{B}^T & \mathbf{D} \end{bmatrix} \begin{Bmatrix} \boldsymbol{\varepsilon}_0 \\ \boldsymbol{\kappa} \end{Bmatrix} \quad (2)$$

The stiffness matrix is built considering an ideal reference structure, as shown in Fig. 4, that consists of a sandwich panel with symmetrical upper and lower laminated skins, which are supposed to be obtained by a lay-up of unidirectional (UD) carbon reinforced plies. A homogeneous lamination sequence is considered with fibers in the spanwise direction. Once the material properties are known, the stiffness contribution of the skin is completely determined by the value of the skin thickness. A laminate stiffness matrix is initially built by considering the UD properties reported in Fig. 4 and negligible core stiffness properties, although the core thickness is taken into account in the evaluation of the bending stiffness, which is represented by submatrix \mathbf{D} in Eq. (2). Thereafter, the requirement for the low membranal stiffness is introduced, and the membranal stiffness in the chord direction is replaced by a significantly lower value. Such a value is set considering the properties of the elastomeric core in the ideal reference structure. It has to be remarked that such a building procedure of the laminate stiffness matrix does not correspond to any specific constructive solution, but it substantially uncouples flexural and membranal stiffness in the chordwise direction and links the chosen values to the properties of

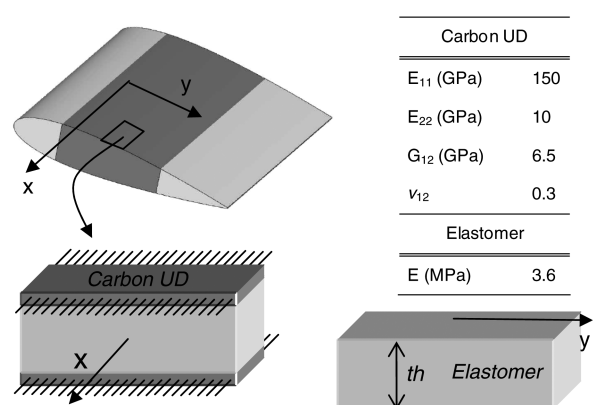


Fig. 4 Idealized reference structure and materials for skin properties.

real materials and geometries. Elastomeric materials can have a wide range of mechanical properties, with Young's moduli varying between 0.01 MPa to 25 MPa [25]. The initial choice, which is adopted in the studies presented in Section IV, consider an elastomeric layer with a Young's modulus of 3.6 MPa and a thickness of 1.5 mm. Such a choice leads to a membranal stiffness in the chord direction of 5.4 N/mm in the plate, representing the skin, which is characterized by the stiffness matrix given in Eq. (2). A thickness of 0.4 mm is chosen for the UD covers. Hence, the geometry of the ideal sandwich structure and the properties of the UD covers and of the elastomer core are used to build the matrix to obtain reasonable values of stiffness.

IV. Structural Response of the Morphing Structure Including a Chiral Wing Box

This section presents a series of FE analyses carried out on wing-box models that embody the morphing sail concept. The analyses evaluated the response of the chiral wing box in simple load conditions. The objective is twofold: the assessment of a possible configuration of the chiral network as well as the investigation of the stiffness properties for such an innovative structural concept. The chiral wing box was defined considering preliminary, nonoptimal, configurations and was also compared with a reference conventional wing box.

A. Configuration of the Morphing Structure and Preliminary 2-D Analyses

A NACA 0018 symmetric airfoil is chosen for the application of the morphing sail. The chord of the profile is set to 1 m. Exploiting the concept presented in Section I, the structure consists of three parts: the leading edge box, a central box with a chiral core, and a trailing-edge box. The technology described in Section III.B is adequate to breed a regular and uniform chiral tessellation, which uses a single type of ligament with a constant length. As a consequence, the airfoil inner volume is filled with a network of equilateral triangles, which schematize the hexachiral unit cell. Two types of filling algorithms are considered, which produce the networks represented in Fig. 5. The first one builds a front that advances in the vertical direction, leading to structures with nodes aligned along horizontal lines, whereas, in the second one, the front advances in the horizontal direction, leading to structures with nodes aligned along vertical lines.

The second approach, shown in Fig. 5b, breeds a network with more nodes on the limiting spars, which are used to connect the chiral structure with the leading and trailing-edge boxes.

Two-dimensional (2-D) models of these structures were developed and analyzed with the Abaqus\Standard FE code [26]. A strip with two elements in the spanwise direction is modeled using linear shell elements. Leading-edge and trailing-edge boxes are considered as rigid bodies, pinned to the fixed reference frame by two hinges. The ligaments are modeled as laminates made of a carbon/epoxy-reinforced fabric plies with the characteristics that are reported in Table 1. The skin is modeled by bidimensional shell elements, directly characterized by means of the stiffness matrix

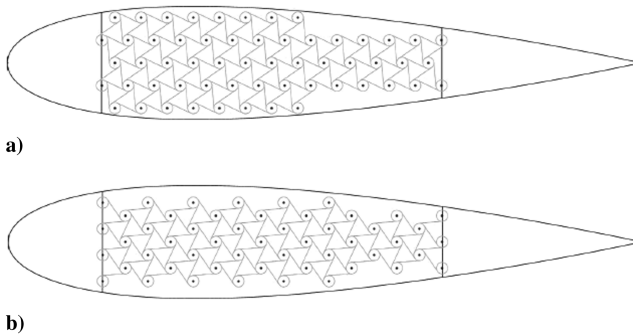


Fig. 5 Typologies of chiral networks obtained by means of the two different filling algorithms.

Table 1 Properties of the ligament material

E_{11} , GPa	56.55
E_{22} , GPa	56.55
v_{21}	0.05
G_{12} , GPa	4.04
Thickness, mm	0.1

reported in Eq. (2), which was built according to the procedure discussed in Section III.C. The transverse shear stiffness of the shell elements has been characterized according to the default settings of the solver code, which uses a combination of the membranal stiffness terms to provide an approximation of transverse stiffness values when no specific calibration is introduced [27]. The introduction of more accurate transverse shear properties would require a definition of the constructive solutions for the morphing skin, which is not included in the objectives of the present work.

Figure 6a shows a detail of the FE model, which is useful to illustrate how the connections between the chiral core and the other parts of the structure are modeled. All of the elements of each chiral node at the boundary of the core are connected to its center by means of rigid beams; then, the skin is attached to such node centers by means of pinned beams, whereas the connection with the leading and trailing-edge spars is obtained by including the node centers into the corresponding rigid bodies.

Numerical tests were carried out on several models to assess the morphing concept and to find the best approach to connect the chiral core to the rigid parts.

Analyses were performed by applying a rotation to the leading or trailing edges, as it is exemplified in Fig. 6b. Preliminary analyses indicated that the net type of Fig. 5b is preferable because the forces that are transmitted between the chiral core and the rigid bodies are distributed among a greater number of nodes. Moreover, the numerical analyses showed that the cylinders should be pinned rather than clamped to the limiting spars to reduce stress concentration on the chiral ligaments.

Finally, preliminary analyses were performed to find the appropriate mesh refinement level and to check the difference between considering linear and geometrically nonlinear solution approaches. According to these simulations, summarized in Fig. 7, acceptable results can be obtained by relatively coarse meshes and by simple linear analyses.

B. Tensile and Torsional Numerical Response with 3-D Finite Element Models

In the selected configuration for three-dimensional (3-D) structural analyses, the chiral core takes up the volume between 21% and 67% of the chord. Considering the nomenclature of Fig. 2, the parameters for this test chiral topology specimen are set to $r = 12$ mm, $L = 38$ mm, and $R = 45$ mm. Composite parts were modeled considering the carbon fabric plies with the properties reported in Table 1. Two lamination sequences were considered for

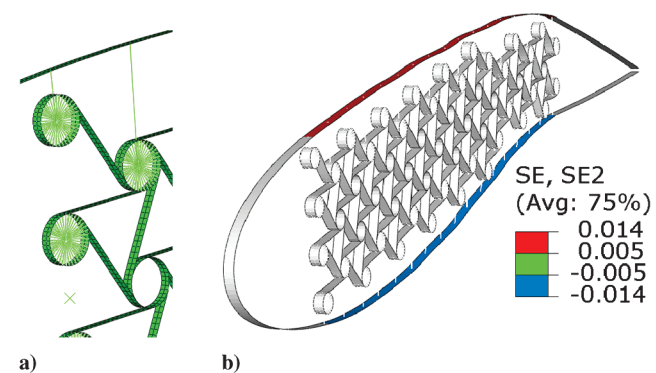


Fig. 6 a) Detail of the modeling technique and b) contour of strain on the skin with an imposed 15 deg trailing edge rotation.

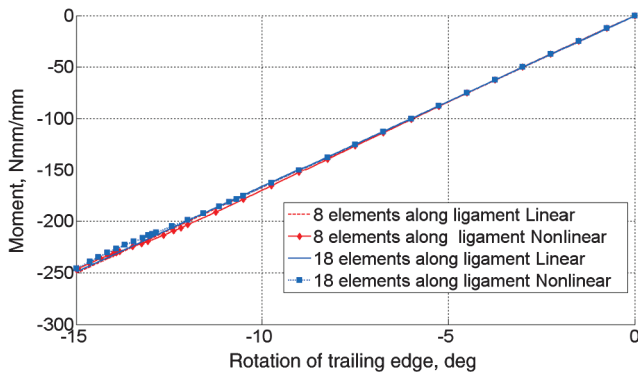


Fig. 7 Comparison of linear and nonlinear analyses at different mesh refinement levels.

the ligaments: a cross-ply sequence $[0]_6$, and a sequence that includes ± 45 oriented plies, namely $[45 -45 0 45 0 -45 45]$. Such sequences will be referred to as cross-ply (CP) and multidirectional (MD) sequences. Because of the fabric properties, both sequences represent symmetrical and equilibrated laminates.

In the 3-D models, the leading-edge and the trailing-edge boxes were modeled as deformable composite parts, made of a symmetrical laminate with the sequence $([0 90 45 -45 0])_s$. Moreover, such boxes were endowed with uniformly spaced internal ribs, which were modeled with the same lamination sequence as the boxes.

As far as the skin is concerned, properties were determined as indicated in Section III.C. A thickness of 1.5 mm was attributed to the elastomeric layer, and 0.4 mm thick laminates of UD carbon were considered for each cover of the equivalent honeycomb panel.

Two FE schemes with a span of 1 m and 2 m were developed, with a mesh refinement level characterized by eight elements along each ligament. First-order shell elements (type S4 [27]) have been used for the chiral core, the leading and trailing edges, and the skin. The number of elements is about 450,000 and 890,000 for the versions with 1 m span and 2 m span, respectively. Static linear analyses have been performed by using the Abaqus/Standard code.

The boundary conditions were changed for each performed analysis. Figure 8 shows the final 3-D model with a span of 1000 mm. For the sake of clarity, the deformable skin is removed in the visualization. The upper panels of the leading-edge and trailing-edge boxes are also removed to show the internal ribs. It can be observed that the sets of skin-core connecting beams and the internal ribs were spaced, respectively, by 166 mm and 250 mm in the spanwise direction.

The cylinders of chiral core can potentially offer a significant contribution to axial and bending stiffness. Nevertheless, if the core must be free to bend in the chordwise direction, cylinders and ligament cannot be clamped at the ends of the morphing surface, unless complicated constraint systems are considered. Hence, a fundamental issue to exploit the potential of chiral wing boxes is represented by the diffusion of loads from the spars into the chiral core.

The tensile numerical tests that are hereby presented were carried out by applying the wing-root constraints that are required by the morphing sail concept. At one end of the structure, the external nodes of the leading and trailing-edge boxes were included in two rigid

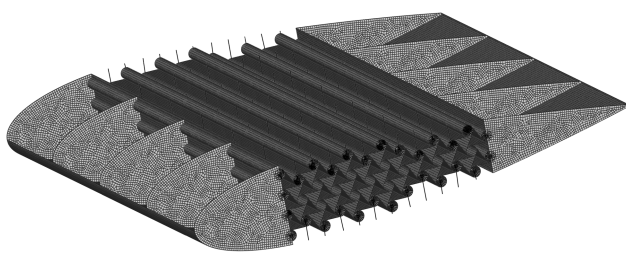


Fig. 8 3-D model of the morphing structure.

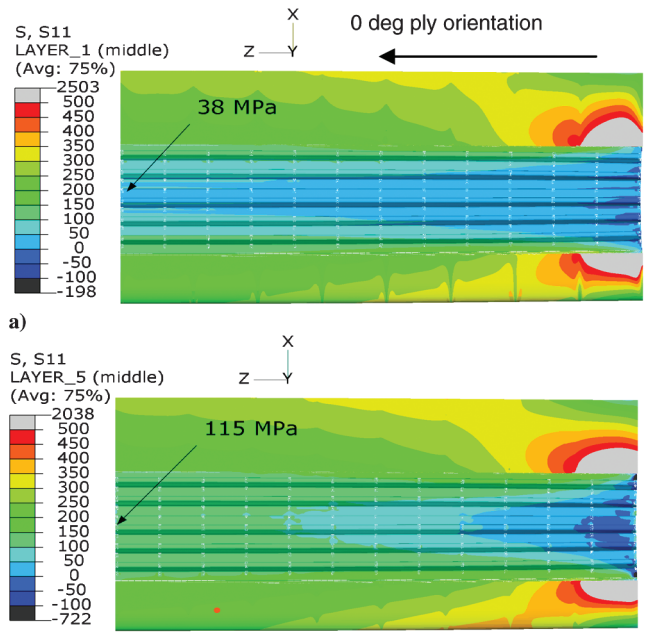


Fig. 9 Contour of normal stress in 0 plies for the a) CP and b) MD model.

bodies, which were connected at the root by two plain hinges. At the opposite end, a stretching of 1 mm was imposed to all of the structural nodes that belong to the final section.

Figure 9 reports the contour of longitudinal stress for two analyses, which were carried out considering a CP and MD lamination sequence for the chiral core, with a 2000 mm span length model. If a CP lamination sequence is adopted, load diffusion is not very efficient, and the central core is slightly and not uniformly loaded. In such a condition, the contribution of the chiral box to axial stiffness is not relevant. When a MD sequence is employed, the presence of ± 45 oriented plies promotes a more rapid diffusion of the load towards the center of the core, which tends to be uniformly loaded after a distance of 1000 mm from the constraint. Such improvements indicate that an appropriate choice of the lamination sequence can enhance the contribution of the chiral core to axial and bending stiffness, even in the most unfavorable constraint conditions.

Three-dimensional models were also employed to assess torsional behavior and stiffness of the morphing sail. The results that were obtained by considering an MD lamination sequence on a 1000 mm span model are presented and compared with a reference structure. Such a structure, which does not have morphing capabilities, is obtained from the designed wing by substituting the deformable central core and skin with a conventional stressed-skin construction, as shown in Fig. 10. In this case, skin and ribs all have the same lamination sequence: $([0 90 45 -45 0])_s$.

The shear centers of both the conventional and the morphing structures were evaluated by a numerical approach. Such a point represents the reference node for a kinematic constraint, which makes all FE nodes of a section rotate as they are rigidly connected to the corresponding shear center, whereas all the other degrees of

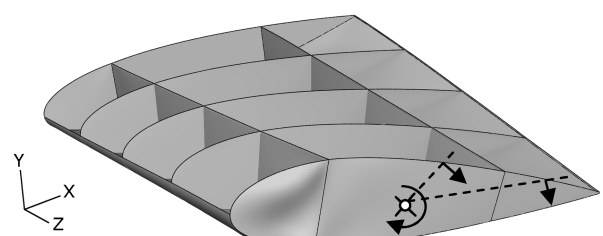


Fig. 10 Model of a conventional stressed-skin structure and torsion kinematic constraint.

Table 2 Torsional stiffness of 3-D models

Model	Torsional stiffness, Nmm/rad	$\Delta\%$ with respect to conventional model
Conventional	$4.021 \cdot 10^8$	-
MD nominal	$2.996 \cdot 10^8$	-25.5%
MD morphing sail constraint	$2.130 \cdot 10^8$	-47.0%
MD morphing sail constraint (reduced skin shear stiffness)	$2.082 \cdot 10^8$	-48.2%

freedom are left free (see Fig. 10) [27]. If such a constraint is applied to both ends of the structure and one of the sections is rotated, the nominal torsional stiffness can be evaluated by the ratio between the reaction torque and the applied rotation. Alternatively, if the root end is constrained by the two plain hinges, a different evaluation is obtained, which takes into account the need of diffusing the stress state into the unconstrained chiral core. Table 2 compares the stiffness of the conventional solution with the ones of the morphing sail in the two constraint conditions.

The nominal torsional stiffness of the morphing structure only differs by 26.2% with respect to the conventional solution. Such a result is mainly due to the stiffness provided by the chiral network, in particular by the more external ligaments. Figure 11 shows the contour of the absolute value of the shear flow in the MD model with nominal constraints. The contribution of deformable skin, which has the shear stiffness of a homogeneous UD laminate oriented in the spanwise direction, is low. The outer ligaments of the chiral core carry a shear flow of about 108 N/mm, whereas shear flows of 118 N/mm and 67 N/mm act in the leading and trailing edge, respectively. The third case in Table 2 is obtained by applying the constraint required by the morphing sail concept, and it shows that, even in such unfavorable conditions, more than 50% of the stiffness of the conventional structure is retained. The final result reported in Table 2 has been obtained by reducing the shear term of the submatrix A of the skin membranal stiffness. In particular, such a term was replaced by the value corresponding to the one of the reference elastomeric core. In conclusion, these tests show how the effects on the torsional stiffness of the structure are limited, and the morphing sail only constrained at the pinned rigid boxes still retains more than 50% of the stiffness of the conventional reference structure.

V. Parameterized Aeroelastic Models

A. Generation of 2-D Chiral Topologies

The previous structural investigation confirmed that a chiral structure represents a valid solution for morphing. It conjugates a tunable chordwise compliance while providing axial and bending stiffness contributions and a significant torsional stiffness.

To design a feasible configuration for the morphing sail that exploits the best from this new concept, it has been decided to tackle the problem by using a numerical optimization procedure applied on a 2-D model, such as the one presented in Section IV.A. In particular, this model is used to investigate the influence on performances of the extension of a chiral wing box (parameters x_1 and x_2 of Fig. 1), the position of the joints (parameters x_{g1} and x_{g2} of Fig. 1), and the chiral cell geometry and materials.

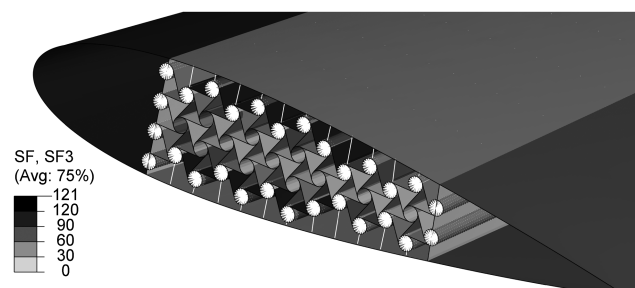


Fig. 11 Absolute value of the shear flow in the torsion analyses with nominal constraints.

The implementation of an automatic parametric generator of the chiral nets was mandatory to adopt a numerical optimization procedure. This task is fulfilled with a set of routines implemented in MATLAB, which take the parameters of the chiral topology, the airfoil geometry, and the amplitude of the chiral box as input. At first, a regular rectangular chiral net is defined through the definition of the node centers into the assigned wing-box extension. Subsequently, the obtained net is intersected with the airfoil shape, and only the internal nodes are kept. Finally, the ligaments that link together the nodes are generated. In this way, the geometry for the FE model is obtained.

B. Static and Dynamic Aeroelastic Modeling

The static and dynamic performances of the morphing sail section must be evaluated by the optimization procedure built to define a feasible set of design parameters. Using the iterative static aeroelastic algorithms shown in Fig. 12, the trim condition is computed. Every iteration starts with the calculation of the pressure distribution over the airfoil with an assigned geometry. The aerodynamic solver used is XFOIL [26], which couples an inviscid potential flow solution with thin boundary-layer corrections. In this way, it is possible to evaluate the occurrence of flow separation caused by large airfoil deformations and estimate the drag forces with a low computational time. The computed loads are transferred into a static FE analysis of the section's structure, which uses the 2-D model generated by the automated procedures already described. The resulting deformed shape obtained by the structural analysis is fed back into the aerodynamic solver until convergence is reached. The convergence is checked by evaluating two different criteria simultaneously: the first based on the norm difference of two consecutive iterations of the FE model nodal displacement vector:

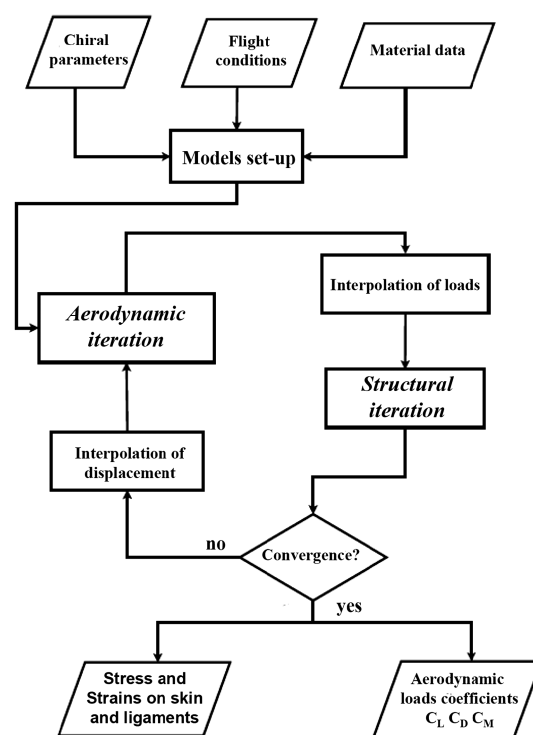


Fig. 12 Block diagram of static aeroelastic algorithm.

$$\frac{\|\mathbf{u}^k - \underline{\mathbf{u}}^{k-1}\|}{\|\mathbf{u}^k\|} < \varepsilon_s \quad (3)$$

and a second based on the difference of the aerodynamic lift coefficient:

$$C_L^k - C_L^{k-1} < \varepsilon_A \quad (4)$$

In this way, the aerodynamic coefficient of the deformed section and the stress and strain status of the structure are computed.

To run the static aeroelastic analyses, it is necessary to transfer the aerodynamic loads on the FE grid and send back the structural displacement on the XFOIL panel discretization. A single interface scheme based on the moving least square approach [28] is used. This approach ensures the conservation of the work exchanged between the two models.

The aeroelastic dynamic response requires a different model to investigate the flutter of the structure. This model must take into account the unsteady aerodynamic forces and inertial property of the section. The calculation of unsteady aerodynamic forces is accomplished with a simple doublet lattice method (DLM), using the solver available in NASTRAN. To obtain the solution on the 2-D section, a 3-D aerodynamic discretization of a rectangular wing with an aspect ratio of 20 is used, but the forces, computed by applying a set of symmetric boundary conditions, are evaluated only in the central section, where the flow is not significantly influenced by the 3-D effects.

To evaluate the dynamic response, a reduced order model (ROM) based on structural normal modes is built using the same structural FE model realized for the evaluation of static performances of the morphing sail. This ROM reduces the number of structural degrees of freedom to the amplitude of the first few low-frequency modes that introduce a significant variation on the aerodynamic loads. Figure 13 shows an example of the first three modes, all characterized by chordwise deformations. Because a 2-D structural model is used to represent a 3-D structure, the sectional mass of the leading-edge and trailing-edge boxes that do not have the same configuration for every wing section as the chiral box (see Fig. 8) has been appropriately scaled. The modes of the 3-D model with a 2000 mm span were also evaluated to verify that all the significant low frequency modes are essentially characterized by chordwise deformations of airfoil, whereas the first wing torsion and bending modes are well above the frequency range. In fact, the resulting first three modes are almost coincident in terms of frequency and mode shapes to those obtained by the 2-D model.

As a result, the structural dynamics is represented by

$$\mathbf{M}_s \ddot{\mathbf{q}} + \mathbf{K}_s \mathbf{q} = q \mathbf{F}_a(\mathbf{q}, \dot{\mathbf{q}}) \quad (5)$$

where \mathbf{q} is the modal coordinates vector, \mathbf{M} and \mathbf{K} are, respectively, the modal mass and stiffness matrices, q is the dynamic pressure, and \mathbf{F}_a is the vector of unsteady generalized aerodynamic forces (GAFs). No structural damping is considered. However, the viscoelastic constitutive law of the rubber components that are expected to be part of the morphing sail skin will introduce a significant structural damping to all modes that show a deformation of the skin. This damping will certainly increase the structural aeroelastic stability, so the choice of neglecting it in this phase can be considered conservative.

The DLM is used to compute the frequency response of the unsteady GAFs associated with the modes shown in Fig. 13, the \mathbf{H}_{am} matrix, that is subsequently converted into a state-space representation using Roger's approach [29,30]. As a result, the GAFs can be represented using the following state-space model:

$$\begin{aligned} \left(\frac{c}{V} \right) \dot{\mathbf{x}}_a &= \mathbf{A}_a \mathbf{x}_a + \mathbf{B}_a \mathbf{q} \\ \mathbf{F}_a &= \mathbf{C}_a \mathbf{x}_a + \mathbf{D}_0 \mathbf{q} + \frac{c}{V} \mathbf{D}_1 \dot{\mathbf{q}} + \left(\frac{c}{V} \right)^2 \mathbf{D}_2 \ddot{\mathbf{q}} \end{aligned} \quad (6)$$

A complete state-space dynamic aeroelastic model can be assembled connecting Eq. (5) with Eq. (6). This model can be used to investigate

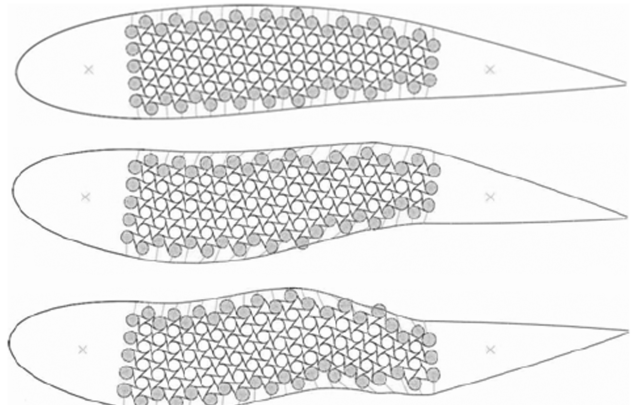


Fig. 13 Chordwise deformation modes of chiral airfoils.

the dynamic stability of the morphing system by looking at the evolution of the coupled system eigenvalues with respect to the dynamic pressure.

VI. Optimization of Performances

A. Formulation of the Optimization Problem

The purpose of the optimization for the morphing sail is to find the set of parameters that maximize the slope of the airfoil lift-curve slope, C_{La} , for the compliant configuration. So, the most appropriate objective function to be used in the optimization process is

$$\mathbf{F}(\mathbf{X}) = \frac{1}{C_{La}} \Big|_{\alpha=0} \quad (7)$$

The design parameters \mathbf{X} , in this case, are a set of topological and material variables. In particular, the response of the morphing airfoil is evaluated as function of: 1) r and L , the geometrical dimensions of the chiral cells (see Fig. 2); 2) x_1 and x_2 , the fore and aft spar positions that limit the extension of the chiral box (see Fig. 1); 3) x_{g1} and x_{g2} , the fore and aft positions of the ground pin points (see Fig. 1); 4) t_c , the thickness of composite laminates used for the ligaments; and 5) D_{skin} , the flexural stiffness of the plate representing the skin in the chordwise direction.

Ligaments are considered laminated with a fabric $[0]_{ns}$ lay-up, with the material properties that have been presented in Table 1. As far as the skin is concerned, it has been observed that the membranal stiffness of the skin negatively influences the morphing performance, and it has been decided to keep its value at a low level. Accordingly, the value of 5.4 N/mm, which was obtained in Section III considering an idealized reference structure, has been fixed in the computations. On the contrary, the flexural stiffness of the skin has been considered a design variable. In the building procedure of the laminate matrix, such a value can be changed by varying the thickness of the UD $[90]_{ns}$ lay-up attributed to the cover of the idealized reference structure, presented in Fig. 4. As the objective of the optimization is indeed the identification of basic stiffness requirements for the skin and not the definition of a constructive solution, the level of flexural stiffness, D_{skin} , should be considered as the actual variable in the optimization process.

The increase of the lift-curve slope is obtained through the elastic modification of the airfoil camber. No constraint on the geometry of camber modifications has been set in place. Nevertheless, the employment of an aerodynamic solver that predicts boundary-layer behavior naturally led the optimizer toward airfoil structures with very smooth camber modifications. Some exceptions have been obtained when the optimizer ended in minimal points characterized by a topology of the chiral box that showed a structural weak point, a sort of virtual hinge point caused by the presence of less chiral nodes at one station chordwise. In these cases, the resulting camber variation was of a bilinear type similar to that of classical airfoils with movable surfaces. However, these solutions have been discarded

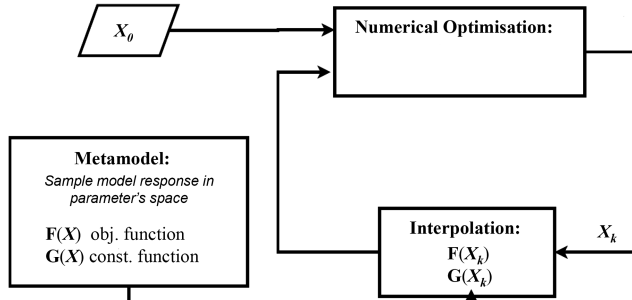


Fig. 14 Numerical optimization strategy based on meta-model constructions.

because they are characterized by an intrinsically weak structural point: the virtual hinge point in the chiral structure.

A large number of structural and aerodynamic simulations are needed for the evaluation of the static and dynamic aeroelastic performances. For this reason, the optimization problem is tackled using the response surfaces approach, to reduce the computational effort required. According to this approach, the performances of the model are approximated using a multidimensional interpolation technique that starts from the knowledge of only a restricted number of solution points evaluated in the space of the acceptable parameters. The procedure adopted is shown in Fig. 14.

The derivative of the airfoil lift curve is obtained by computing the static aeroelastic configuration at several angles of attack around the position $\alpha = 0$ and then computing the value by finite difference.

B. Constraints

To define a feasible space for the solution, it is required to add several constraints to the optimization process. These constraints can be classified as structural, aerodynamic, and aeroelastic.

The essential structural constraint is the verification that the designed structure can stand the ultimate limit load without fracture or failures. The limits referred to the two main failure modes of the hexachiral units, which have been described in Section III and are sketched in Fig. 15, are adopted to include two basic structural constraints in the optimization problem. The possibility of debonding due to ligament unwinding is considered by evaluating the bending moment at the root of the ligament, and the risk of bending failure of the ligament is taken into account by recovering the maximum longitudinal strain on the ligament surface. It is assumed that the limit unwinding bending moment per unit width (M_b/L)_{lim} and the maximum strain at bending failure ε_{lim} are not significantly dependent on the geometry of the cell so that the values obtained experimentally for the unit hexachiral cells presented in Bettini et al. [12] have been retained here, too.

Accordingly, the optimization constraint for the debonding failure mode, which occurred in the tensile tests of the chiral units, is formalized as in Eq. (8):

$$\left(\frac{M_b}{L}\right)^{\text{TENSION}} \leq k \left(\frac{M_b}{L}\right)_{\text{lim}} \quad (8)$$

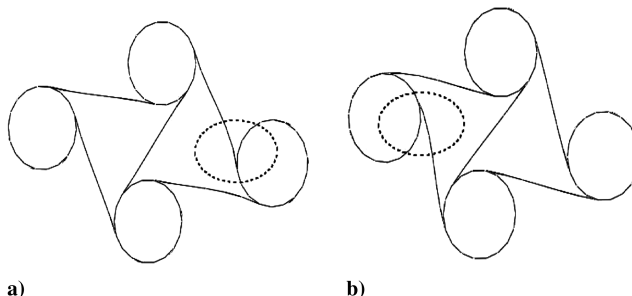


Fig. 15 Chiral cell's deformation modes: a) unwind and b) wind.

where M_b/L is the moment per unit width recovered in the shell elements of the ligaments and $k = 0.8$ is a factor of safety, introduced to take into account simplifications and inaccuracies in the FE model. The limit value $(M_b/L)_{\text{lim}}$ has been fixed to 16.7 N, according to the results obtained in Bettini et al. [12].

For the bending failure of the ligaments, which characterized the compressive response of the chiral units, a maximum allowable winding bending moment is obtained within the assumption of linear elastic material, by considering the limit strain on the ligament surface, as it is formalized in Eq. (9):

$$\left(\frac{M_b}{L}\right)^{\text{COMP}} \leq k \left(\frac{Eh^2\varepsilon_{\text{lim}}}{6}\right) \quad (9)$$

where E is the material Young's modulus, h is the ligament thickness, k is a factor of safety, set again at 0.8, and a limit strain of $\varepsilon_{\text{lim}} = 0.014$ is considered based on the strain gauge acquisitions reported in Bettini et al. [12]. Tensile and compressive failure indices are selected depending on the sign of distance variation between the two nodes connected by the ligament.

The aerodynamic constraints are added to obtain a proper behavior of the airflow that surrounds the airfoil. An excessively compliant structure runs the risk of going into fully separated conditions at high angles of attack due to large chordwise bending of the airfoil. For this reason, it has been assigned a minimum increment of the lift coefficient of the compliant airfoil at the maximum angle of attack

$$\Delta C_L(\alpha_{\max}) = C_L^{\text{elast}}(\alpha_{\max}) - C_L^{\text{rigid}}(\alpha_{\max}) \quad (10)$$

which has to be satisfied. In this case, the maximum angle of attack has been fixed at 10 deg.

For some choices of the flexural stiffness of the skin, it is possible to end up in situation where the deformed airfoil assumes a wavy shape, visible in the deformed airfoil of Fig. 6b. This, in turn, influences the pressure distribution, giving rise to oscillation in the pressure coefficient distribution, as shown in Fig. 16. To avoid the possibility of ending up with a structural configuration that shows these behaviors, it has been necessary to add a constraint to reject them. To do so, it is necessary to detect automatically a high-frequency spatial oscillation in the pressure coefficient distribution. This can be obtained by looking at the variance of the local pressure coefficient distribution with respect to a smoothed pressure coefficient \hat{C}_{pi} (through a least mean square polynomial reconstruction), i.e.,

$$\sigma_{Cp}^2 = \frac{1}{N-1} \sum_{i=1}^N (C_{pi} - \hat{C}_{pi})^2 \quad (11)$$

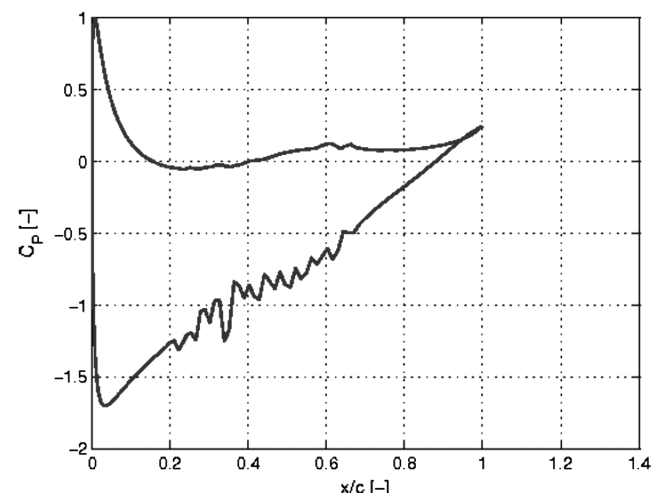


Fig. 16 Pressure coefficient due to wavy skin deformation on the upper surface.

where N is the number of stations where the pressure coefficient is evaluated. This variance must be below a limit value to avoid configurations with highly oscillating pressure distributions. So, if the structural deformation of the skin causes a too much oscillating pressure distribution, the configuration is rejected.

Finally, an aeroelastic constraint is added to avoid possible incurrence of detrimental aeroelastic instability in the range of design speed for the system. In this case, the g -damping associated with each eigenvalue of the aeroelastic system that represents the dynamic response of the morphing airfoil is constrained to be below an assigned negative threshold. The eigenvalues of the system obtained joining Eqs. (5) and (6) are computed using the continuation technique presented in Cardani and Mantegazza [31]. The maximum g -damping of all the elastic modes in the operative speed range considered is constrained to be below an assigned value.

C. Meta-Model Reconstruction

An important aspect of the response surface method is the definition of the behavior of the model through only few evaluations of functions in the parameter space. This operation is essentially an interpolation of the available data in a multidimensional domain. To avoid the possibility of dealing with pathologically complex surfaces, it is chosen to represent both the objective function and each constraint as independent meta-models. In this case, it is necessary to build the hypersurfaces that represent the objective function and the five

constraints in the eight-dimensional parameter space. Because no previous knowledge on the shape of these hypersurfaces was available, it has been chosen to build the meta-models using the neural network (NN) approach [32]; NN is known to be a universal nonlinear approximator. The initial parameter set to be evaluated is defined using the classical Latin hypercube sampling technique; then, several additional points are added locally to reduce the error between the exact surface and the meta-models. Some results are shown in Fig. 17. Even if the surfaces are multidimensional, restriction to 2-D spaces is showed, keeping all parameters but the two shown fixed. It is interesting to see that the lift-curve slope is at a maximum for chiral cells characterized by large ligament lengths with a weaker dependency from the center radius when L is large. Figure 17b shows that the performance is essentially influenced by the position of the rear spar, whereas Fig. 17c suggests that both the compliance of the chiral structure and of the skin concur to realize the performance.

By employing these meta-models, the numerical optimization procedure is performed using the classical constrained gradient-based algorithm implemented in MATLAB through the function "fmincon".

D. Results and Discussion

The optimization is performed considering an operative speed $V = 50$ m/s for the morphing system. This choice was made due to the operative speed of one of the wind tunnels of the Department of

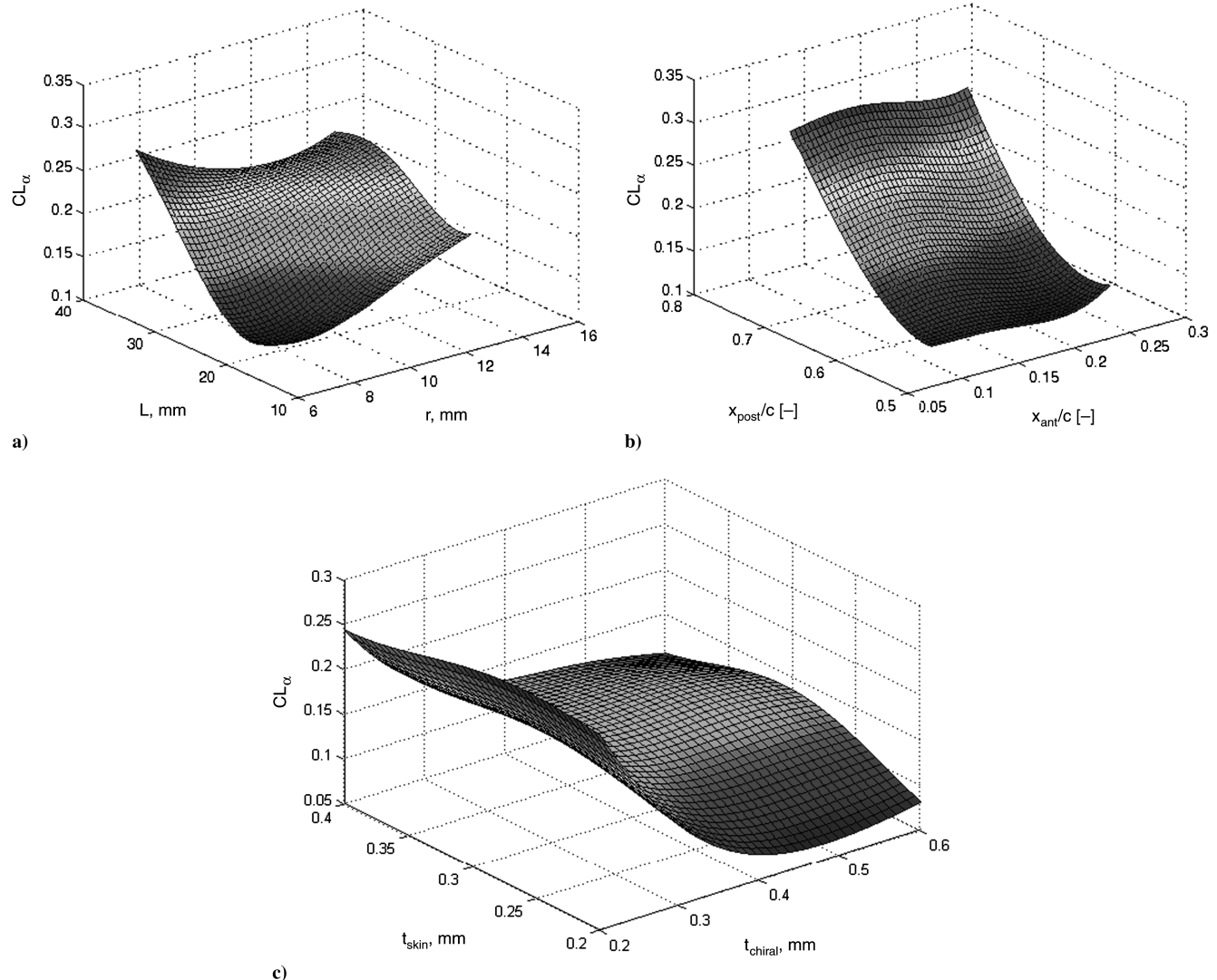


Fig. 17 2-D response surfaces evaluated using NN approach. Dependence of lift-curve slope from a) chiral geometry parameters, b) position of the anterior and posterior spars, and c) thickness of skin and of the inner chiral structure.

Table 3 Optimization parameter ranges and optimal values

Parameter	Minimum	Maximum	Optimal
x_1/c	0.075	0.225	0.200
x_2/c	0.540	0.900	0.900
r , mm	7.200	14.400	10.300
L , mm	18.750	37.500	19.300
x_{g1}/c	0.0500	0.95 x_1/c	0.120
x_{g2}/c	1.05 x_2/c	0.950	0.780
t_c , mm	0.2	1	0.232
D_{skin} , Nmm	183	1010	618

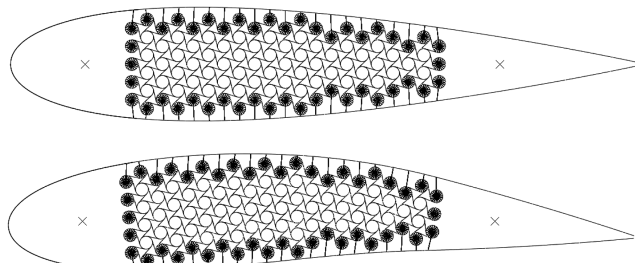


Fig. 18 Optimized chiral wing section a) undeformed and b) deformed at $\alpha = 10$ deg.

Aerospace Engineering of Politecnico di Milano, which is the most probable candidate to perform future experimental testing.

The parameter ranges used during the optimization process are shown in Table 3. Figure 18 presents the optimized section geometry, whereas Table 3 shows the associated parameter values of the optimal configuration. The optimal ligament thickness is very low, due to the choice of a limited operative speed. The response of the chiral core is governed by the bending stiffness of the ligament in the chordwise direction that, according to classical plate theory, corresponds to 58.99 Nmm for the optimized ligament. An equivalent bending stiffness could be obtained with a thicker ligament by varying the lamination sequence or changing the type of material to consider a thicker and more technologically feasible ligament. It should be noted that, according to the results shown in Section IV, a multidirectional laminate is to be preferred for ligaments to enhance the contribution of the core to axial and torsional stiffness.

The undeformed and the deformed shapes for the optimal solution are compared in Fig. 18. It can be observed that the sail-like behavior is obtained without significant distortions on the skin surface.

The mean line of the deformed shape is also properly bent, without abrupt changes in slope and a smooth curvature variation. As a

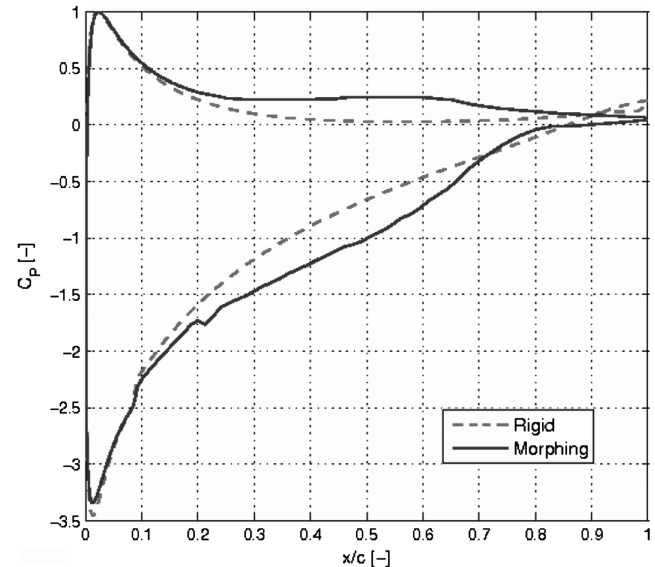


Fig. 19 Pressure coefficient distribution over optimized airfoil at $\alpha = 10$ deg.

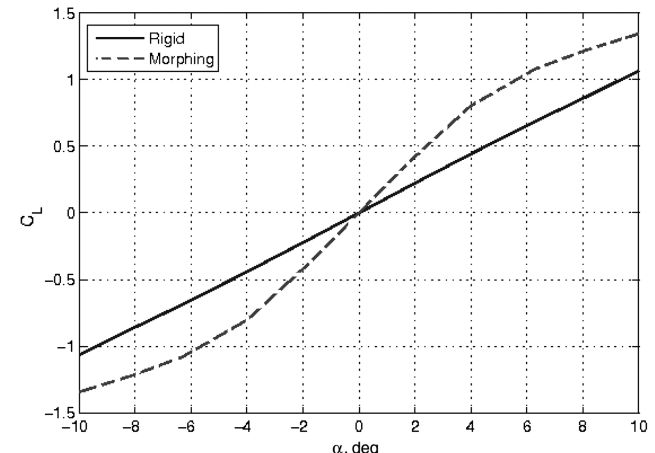


Fig. 20 $CL-\alpha$ curve for the rigid and the optimized morphing airfoil.

consequence, a very regular pressure distribution over the external skin is obtained at a maximum angle of attack, as shown in Fig. 19. The increment of lift coefficient with respect to the undeformed case is the result of contributions coming both from the top and bottom

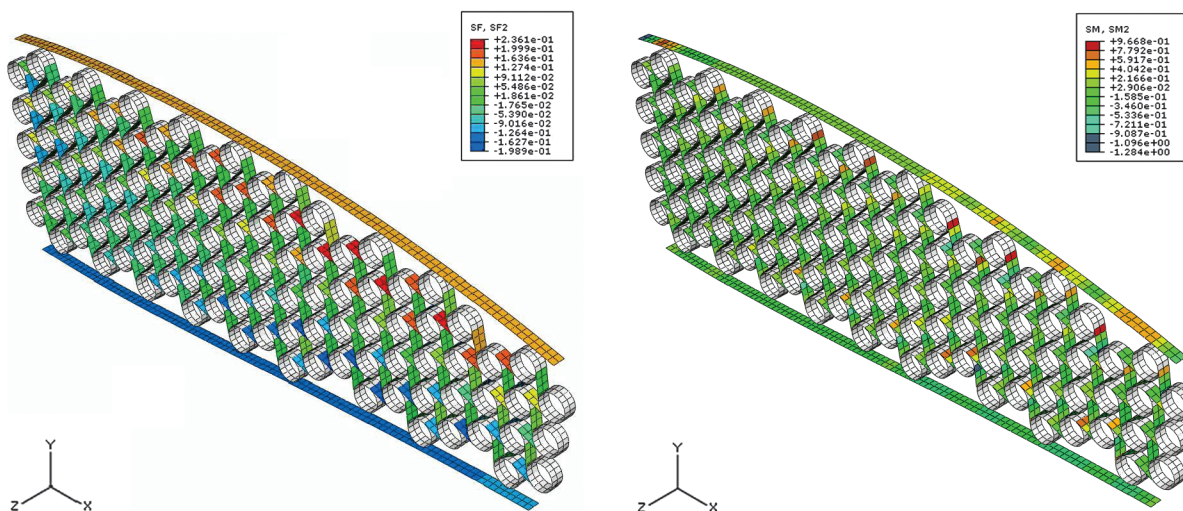


Fig. 21 Stress distributions due to axial load (left) and bending moment (right).

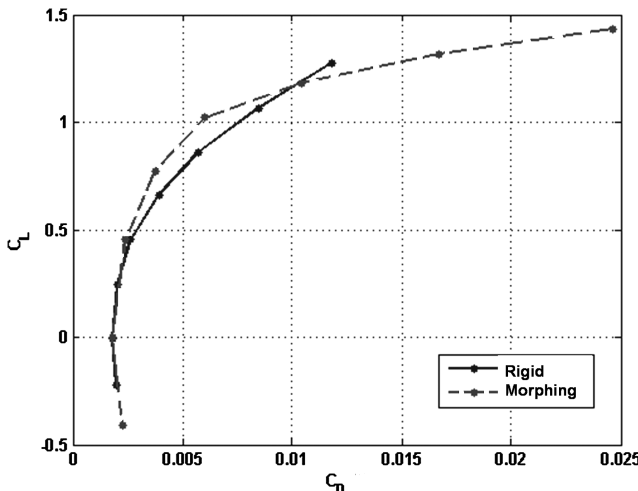


Fig. 22 Airfoil polar curves: comparison between the reference airfoil and the morphing airfoil.

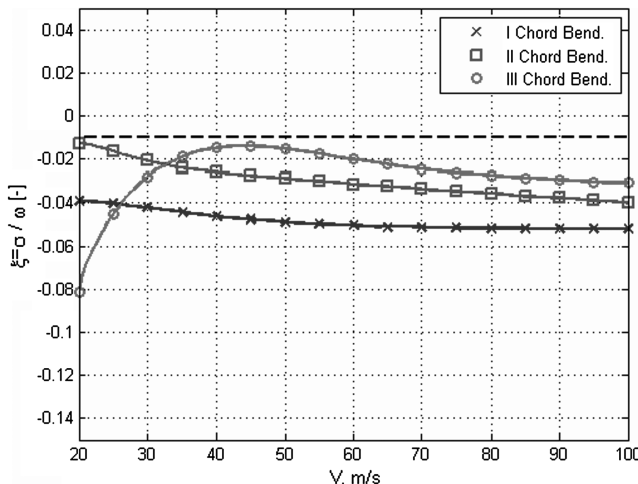


Fig. 23 g -damping factor for the first three structural modes.

surfaces; it is the central part of the airfoil where these variations mainly occur. The $C_{L\alpha}$ -curve in Fig. 20 shows that, for low angles of attack, the $C_{L\alpha}$ is almost doubled. For values of α higher than 6 deg., a reduction of the slope is observed due to the beginning of a smooth separation at the trailing edge.

The chiral structural box has good stress distribution, which respects the structural constrains imposed during the optimization, without stress concentrations that could lead to excessive local deformations (see Fig. 21). The polar curve presented in Fig. 22 shows that the efficiency of the airfoil is improved with the morphing airfoil up to a lift coefficient of about 1.2. To verify the aeroelastic behavior of the structure, the damping coefficient of the first five structural aeroelastic modes were evaluated for the present configuration.

Figure 23 shows the g -damping of the first three modes that have the form shown in Fig. 13. The dashed black line represents the value of the constraint imposed during the optimization that is fixed to a value of $g = -0.01$ and that is fulfilled by the proposed configuration in the range of operative speed investigated. As expected, the aeroelastic constraint is crucial and limits the performance because the obtained solution is almost on the constraint surface.

VII. Conclusions

The paper presented an innovative concept defined as the morphing sail, which can be used to increase the lift-curve slope and the airfoil efficiency. The concept is entirely passive and exploits

only aeroelastic effects to obtain the desired behavior. The studies presented have been based on the adoption of a manufacturing technology for composite chiral elements that was assessed in a previous work.

The innovative chiral topology has been exploited for the structure to obtain the necessary properties that allow the wing morphing while avoiding detrimental structural and aeroelastic effects. Such a result is related to the peculiar properties of the chiral honeycomb, which have been assessed considering bidimensional and 3-D FEM models of the proposed solutions. Despite the chordwise compliance, the contribution of the chiral topology to the torsional and axial stiffness of the wing is not negligible and can be optimized by selecting and possibly grading the most suitable lamination sequence. As far as this aspect is concerned, the work confirms that the interesting properties of chiral topologies can be further enhanced by exploiting the properties of anisotropic laminates.

The design optimization procedure allowed identifying a preliminary design that shows very promising performances. The lift-curve slope has been almost doubled at a low flight velocity, increasing the maximum lift coefficient in the considered range of angles of attack and the efficiency at low angles of attack. Additionally, better performances have been obtained without causing the rise of dynamic aeroelastic problems. These results show the great potential of this peculiar structural topology. In future applications of this concept, it will be possible to trade off a portion of these high performances obtained with the possibility to consider additional requirements, either aerodynamic, aeroelastic, structural, or technological, to the design. Future development will soon consider possible means of activation, at least to prevent undesired behaviors in situations not considered in this study. However, low energy consumption could be expected if the basic, most important performances are obtained without recurring to means of activation. Furthermore, future developments may include multi-objective optimizations that consider the maximization of performance joined with the minimization of structural weight to understand what kind of trade off can be found between these two objectives.

Many technological details related to the manufacturing of a morphing sail prototype have been addressed in a previous work. Although a constructive solution for the morphing skin is not included in the present work, the followed methodological approach, based on the adoption of a generalized stiffness matrix, led to a clear definition of the requirements for such an important feature of the morphing concept.

Globally, this application has shown the great potential of chiral structures applied to wing morphing.

References

- [1] Anderson, J. D., *A History of Aerodynamics and its Impact on Flying Machines*, Cambridge Univ. Press, New York/London/ Cambridge, England, U.K., 1999.
- [2] McGowan, A. R., Cox, D. E., Lazos, B. S., Waszak, M. R., Raney, D. L., Siochi, E. J., and Pao, P. S., "Biologically Inspired Technologies in NASA's Morphing Project," *Proceedings of SPIE Smart Structures and Materials Conference*, International Society for Optical Engineering, Vol. 5051, No. 1, San Diego, CA, Mar. 2003.
- [3] Parker, H. F., "The Parker Variable Camber Wing," NACA Rept. 77, 1920.
- [4] Austin, F., Rossi, M. J., Van Nostrand, W., Knowles, G., and Jameson, A., "Static Shape Control for Adaptive Wing," *AIAA Journal*, Vol. 32, No. 9, 1994, pp. 1895–1901.
doi:10.2514/3.12189
- [5] Strelc, J. K., Lagoudas, D. C., Khan, M. A., and Yen, J., "Design and Implementation of a Shape Memory Alloy Actuated Reconfigurable Airfoil," *Journal of Intelligent Material Systems and Structures*, Vol. 14, No. 4, 2003, pp. 257–274.
doi:10.1177/1045389X03034687
- [6] Couto, D., Brailovski, V., and Terriault, P., "Optimized Design of an Active Extrados Structure for an Experimental Morphing Laminar Wing," *Aerospace Science and Technology*, Vol. 14, 2010, pp. 451–458.
doi:10.1016/j.ast.2010.01.009
- [7] Campanile, L. F., and Sachau, D., "The Belt-Rib Concept: a Structronic Approach to Variable Camber," *Journal of Intelligent Material Systems*

- and Structures*, Vol. 11, No. 3, 2000, pp. 215–224.
- [8] Monner, H. P., “Realization of an Optimized Wing Camber by Using Form-Variable Flap Structures,” *Aerospace Science and Technology*, Vol. 5, No. 7, 2001, pp. 445–455.
doi:10.1016/S1270-9638(01)01118-X
- [9] Renken, J. H., “Mission Adaptive Wing Camber Control System for Transport Aircraft,” *3rd Applied Aerodynamics Conference*, AIAA Paper 1985-5006, Colorado Springs, CO, 14–16 Oct. 1985.
- [10] Bornengo, D., Scarpa, F., and Remillat, C., “Evaluation of Hexagonal Chiral Structure for Morphing Airfoil Concept,” *Journal of Aerospace Engineering*, Vol. 219, 2005, pp. 185–192.
doi:10.1243/095441005X30216
- [11] Spadoni, A., and Ruzzene, M., “Numerical and Experimental Analysis of The Static Compliance of Chiral Truss-Core Airfoils,” *Journal of Mechanics of Materials and Structure*, Vol. 2, No. 5, 2007, pp. 965–981.
doi:10.2140/jomms.2007.2.965
- [12] Bettini, P., Airolidi, A., Sala, G., Di Landro, L., Ruzzene, M., and Spadoni, A., “Composite Chiral Structures for Morphing Airfoils: Numerical Analyses and Development of a Manufacturing Process,” *Composites: Part B—Engineering*, Vol. 41, No. 2, 2010, pp. 133–147.
doi:10.1016/j.compositesb.2009.10.005
- [13] Etkin, B., *Dynamics of Atmospheric Flight*, Wiley, New York, 1972.
- [14] Lakes, R. S., “Deformation Mechanisms in Negative Poisson’s Ratio Materials: Structural Aspects,” *Journal of Material Science and Technology*, Vol. 26, 1991, pp. 2287–2292.
- [15] Prall, D., and Lakes, R. S., “Properties of a Chiral Honeycomb with a Poisson’s Ratio of -1 ,” *International Journal of Mechanical Sciences*, Vol. 39, No. 3, 1997, pp. 305–314.
doi:10.1016/S0020-7403(96)00025-2
- [16] Martin, J., Heyder-Bruckner, J. J., Remillat, C., Scarpa, F., Potter, K., and Ruzzene, M., “The Hexachiral Prismatic Wingbox Concept,” *Physica Status Solidi B*, Vol. 245, No. 3, 2008, pp. 570–577.
doi:10.1002/pssb.200777709
- [17] Alderson, A., Alderson, K. L., Attard, D., Evans, K. E., Gatt, R., Grima, J. N., Miller, W., Ravirala, N., Smith, C. W., and Zied, K., “Elastic Constants of 3-, 4- and 6-Connected Chiral and Anti-Chiral Honeycombs Subject to Uniaxial In-Plane Loading,” *Composites Science and Technology*, Vol. 70, 2010, pp. 1042–1048.
doi:10.1016/j.compscitech.2009.07.009
- [18] Abramovitch, H., Burgard, M., Edery-Azulay, L., Evans, K. E., Hoffmeister, M., Miller, W., Scarpa, F., Smith, C. W., and Tee, K. F., “Smart Tetrachiral and Hexachiral Honeycomb: Sensing and Impact Detection,” *Composites Science and Technology*, Vol. 70, 2010, pp. 1072–1079.
doi:10.1016/j.compscitech.2009.07.017
- [19] Miller, W., Smith, C. W., Scarpa, F., and Evans, K. E., “Flatwise Buckling Optimization of Hexachiral and Tetrachiral Honeycombs,” *Composites Science and Technology*, Vol. 70, 2010, pp. 1049–1056.
- doi:10.1016/j.compscitech.2009.10.022
- [20] Gandhi, F., and Anusonti-Inthra, P., “Skin Design Studies for Variable Camber Morphing Airfoils,” *Smart Materials and Structures*, Vol. 17, 2008, pp. 1–8.
- [21] Bubert, E. A., Woods, B. K. S., Kothera, C. S., and Wereley, N. M., “Design and Fabrication of a Passive 1-D Morphing Aircraft Skin,” *49th AIAA/ASME/ASCE/AHS/ASH Structures, Structural Dynamics, and Materials Conference*, AIAA Paper 2008-2045, Schaumburg, IL, 2008.
- [22] Thill, C., Etches, J. A., Bond, I. P., Potter, K. D., Weaver, P. M., and Wisnom, M. R., “Investigation of Trapezoidal Corrugated Aramid/Epoxy Laminates Under Large Tensile Displacements Transverse to Corrugation Direction,” *Composites Part A: Applied Science and Manufacturing*, Vol. 41, 2010, pp. 168–176.
doi:10.1016/j.compositesa.2009.10.004
- [23] Yokozeki, T., Taked, S., Ogasawara, T., and Ishikawa, T., “Mechanical Properties of Corrugated Composites for Candidate Materials of Flexible Wing Structures,” *Composites Part A: Applied Science and Manufacturing*, Vol. 37, No. 4, 2006, pp. 1578–1586.
- [24] Thill, C., Etches, J. A., Bond, I. P., Potter, K., and Weaver, P., “Morphing Skins,” *The Aeronautical Journal*, Vol. 112, No. 1129, Mar. 2008, pp. 117–139.
- [25] *Polymer Data Handbook*, edited by J. E. Mark, Oxford Univ. Press, Oxford, England, U.K./New York, 1999.
- [26] Drela, M., “XFOIL: An Analysis and Design System for Low Reynolds Number Airfoils,” *Conference on Low Reynolds Number Airfoil Aerodynamics*, Univ. of Notre Dame, Notre Dame, IN, June 1989, pp. 1–12.
- [27] Abaqus, *Analysis and User’s Manual*, Ver. 6.7. Dassault Systèmes, Waltham, MA, 2007.
- [28] Quaranta, G., Maserati, P., and Mantegazza, P., “A Conservative Mesh-Free Approach for Fluid-Structure Interface Problems,” *Computational Methods for Coupled Problems in Science and Engineering*, edited by M. Papadrakakis, E. Onate, and B. Schrefler, Centro Internacional de Métodos Numéricos en Ingeniería, Barcelona, Spain, 2005, pp. 1–22.
- [29] Roger, K. L., “Airplane Math Modeling Methods for Active Control Design,” AGARD, CP 228, Aug. 1977.
- [30] Mattaboni, M., Quaranta, G., and Mantegazza, P., “Active Flutter Suppression for a Three-Surface Transport Aircraft by Recurrent Neural Networks,” *Journal of Guidance, Control, and Dynamics*, Vol. 32, No. 4, 2009, pp. 1295–1307.
doi:10.2514/1.40774
- [31] Cardani, C., and Mantegazza, P., “Continuation and Direct Solution of the Flutter Equation,” *Computers and Structures*, Vol. 8, April 1978, pp. 185–192.
doi:10.1016/0045-7949(78)90021-4
- [32] Nelles, O., *Nonlinear System Identification from Classical Approaches to Neural Networks and Fuzzy Model*, Springer-Verlag, Berlin/New York/Heidelberg, 2001.